JCTC Journal of Chemical Theory and Computation

Letter

pubs.acs.org/JCTC

A Coarse-Grained Model of Unstructured Single-Stranded DNA Derived from Atomistic Simulation and Single-Molecule Experiment

Christopher Maffeo,[†] Thuy T. M. Ngo,[‡] Taekjip Ha,[†,§] and Aleksei Aksimentiev*[,∥,⊥]

[†]Department of Physics, University of Illinois at Urbana−Champaign, Urbana, Illinois, United States

[‡]Center for Biophysics and Computational Biology, University of Illinois at Urbana−Champaign, Urbana, Illinois, United States

[§]The Howard Hughes Medical Institute, Chevy Chase, Maryland, United States

[∥]Department of Physics, University of Illinois at Urbana−Champaign, Urbana, Illinois, United States

[⊥]Beckman Institute for Advanced Science and Technology, University of Illinois at Urbana−Champaign, Urbana, Illinois, United States

Supporting Information

ABSTRACT: A simple coarse-grained model of single-stranded DNA (ssDNA) was developed, featuring only two sites per nucleotide that represent the centers of mass of the backbone and sugar/base groups. In the model, the interactions between sites are described using tabulated bonded potentials optimized to reproduce the solution structure of DNA observed in atomistic molecular dynamics simulations. Isotropic potentials describe nonbonded interactions, implicitly taking into account the solvent conditions to match the experimentally determined radius of gyration of ssDNA. The model reproduces experimentally measured force−extension dependence of an unstructured DNA strand across 2 orders of magnitude of the applied force. The accuracy of the model was confirmed by measuring the end-to-end distance of a dT_{14} fragment via FRET while stretching the molecules using optical tweezers. The model offers straightforward generalization to systems containing double-stranded DNA and DNA binding proteins.

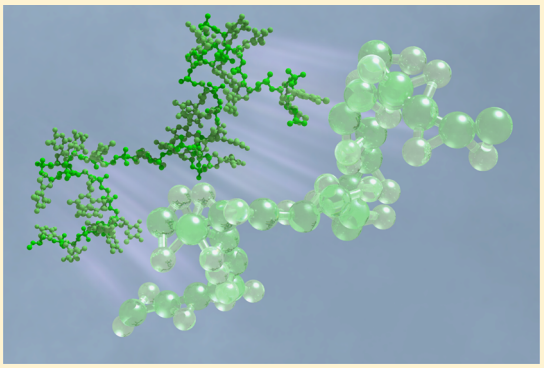

It has become apparent that physical properties of DNA can play a fundamental role in its biological function and can determine the utility of DNA for nanotechnological applications.[1−3] Although the genetic code is stored in double-stranded form, it is the single-stranded form of DNA that plays active roles in central biological processes such as transcription, replication, and DNA repair.[4−7] The emerging field of DNA nanotechnology exploits self-assembly of single-stranded DNA (ssDNA) to create novel nanostructures[8] where DNA is used as a structural element,[9,10] functionalization and assembly agent,[11,12] transport system,[13] etc. Thus, ssDNA is ubiquitous in biology and bio(nano)technology, yet much less is known about its properties in comparison to double-stranded DNA (dsDNA).

Computer simulations can provide detailed insights into the structure, dynamics, and energetics of a biological or nanotechnological system.[14−16] In this regard, all-atom molecular dynamics (MD) simulations that explicitly represent every atom of the system can offer the most detailed account of the system's inner workings.[17,18] However, all-atom MD simulations are currently limited to time scales that are short in comparison to the relaxation time scales of even quite small ssDNA molecules.[19] By describing DNA using a less detailed, "coarse-grained" model, the time scale accessible to simulation can be significantly expanded.[20−22]

All coarse-grained (CG) models of DNA feature coarse-grained interaction sites, which typically represent groups of atoms on the nucleic acid. Having many interaction sites,[23−26] aspherical sites",[27,28] or multibody nonbonded potentials[25] can often enhance the accuracy of the model, usually at the cost of computational performance and/or portability to existing MD codes. Potentials describing interactions between sites are usually obtained by a "top-down" approach,[26−32] in which functional forms are assumed with parameters typically assigned by hand to match experimental observables such as the dsDNA structure and/or thermodynamic melting data. In some cases, the single-stranded DNA of such models has exhibited clear signs of overoptimization to the dsDNA conformation.[30] The alternative "bottom-up" approach to parametrization usually involves systematic optimization of interaction parameters to replicate features observed in atomistic[23,24,33−35] or quantum mechanical[23,36] simulations. Some models fall between the usual classifications by employing "bottom-up" style optimization to match structural distributions from experimentally obtained atomic structures.[25,37] Each approach to parametrization has its drawbacks. Top-down models rely on physical intuition, trial-and-error, and (typically) low spatial and

Received: March 5, 2014
Published: June 3, 2014

   dx.doi.org/10.1021/ct500193u | J. Chem. Theory Comput. 2014, 10, 2891−2896

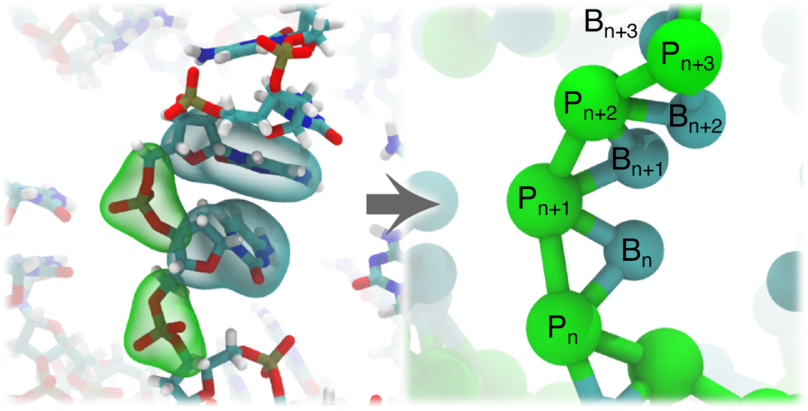

Figure 1. Scheme used to map atoms onto coarse-grained beads. The left panel shows a portion of an all-atom model of ssDNA. The backbone/phosphate and sugar/base atoms of two nucleotides are enclosed by green or cyan semitransparent surfaces, respectively. The enclosed groups of atoms are mapped onto the P (backbone/phosphate) and B (sugar/base) beads, which are shown in the right panel as green and cyan spheres, respectively.

temporal resolution experimental measurements to describe interactions. Bottom-up models rely on expressiveness of the underlying atomic force field, which have historically been corrected many times for various deficiencies.

Although many models of DNA are capable of representing the single-stranded form,[23,24,26−28,32−34,36,38] the existing coarse-grained models of DNA have been foremost optimized to reproduce the properties of the double-stranded form.[23,24,26−28,32−36,38] Validation of the single-stranded properties produced by DNA models against experimental observables has been sparse. Because RNA structures typically contain a significant amount of single-stranded material, we may expect that CG models of RNA[25,37] may better represent single-stranded nucleic acid conformations. However, the properties of ssRNA and ssDNA differ significantly in solution.[39]

We have developed a simple, CG model of unstructured ssDNA. Although we have used a homopolymer of thymine nucleotides as a target for our parametrization, our model can describe any single-stranded DNA lacking a secondary structure. In our model, each nucleotide is represented using two interaction sites, B (base) and P (backbone/phosphate) beads, shown schematically in Figure 1. The interactions between beads are described through interaction potentials tabulated to accurately reproduce the conformations of ssDNA observed in all-atom simulations. The part of the potentials that describes chemical bonds between DNA atoms—bonded potentials—explicitly specifies pairwise interaction of each B bead with two neighboring P beads and also includes four three-bead angle terms and three four-bead dihedral angle terms. The three nonbonded potentials describe interactions between one P and one B bead, two P beads, and two B beads using 1−3 exclusions: the nonbonded potential is zero between beads separated by one or two bonds. The solvent surrounding the DNA is modeled implicitly through a Langevin thermostat and ion concentration-dependent nonbonded potentials. Supporting Information Figures S1, S2, S4, and S5 illustrate the CG potentials of our model.

To obtain CG potentials that are consistent with the all-atom model, we performed a set of reference all-atom MD simulations of a dT_{60} strand submerged in 100 and 1000 mM NaCl electrolytes. All our atomistic simulations employed the CHARMM36 force field,[40] which, according to a recent report, represents conformational dynamics of ssDNA more accurately than the AMBER force field.[18] We used custom corrections to vdW interactions of DNA phosphate oxygens and sodium ions[41] to accurately describe the ionic atmosphere of DNA.[42] A full description of the reference simulations is provided in the Supporting Information.

The resulting all-atom trajectories (9.6 μs of aggregate simulation time) were converted into our CG representation (P and B beads). For a given nucleotide, the P bead represented the O5T′, O5′, P, O1P, O2P, and C5′ atoms of that nucleotide and the C3′ and O3′ atoms of the adjacent nucleotide such that the bead was roughly centered on the phosphorus group of the DNA backbone. The remaining atoms of the nucleotide were mapped onto the B bead. For both types of beads, the conversion procedure was done by computing the center of mass of the respective groups of atoms; hydrogen atoms were neglected during the conversion procedure.

An initial guess for each CG potential was obtained via Boltzmann inversion of the corresponding distribution extracted from the CG-mapped all-atom trajectory. The effect of ion concentration was taken into account by introducing two sets of CG potentials (for 100 and 1000 mM electrolytes) parametrized using the corresponding all-atom trajectories. Using a CG system identical in composition and size to the all-atom one, the bonded—but not nonbonded—potentials were refined by performing 30 iterations of the iterative Boltzmann inversion (IBI) procedure. In IBI, the CG potentials are iteratively adjusted until the distributions obtained from CG simulations converge to the target all-atom distributions, see Supporting Information for details.

Upon completion of the IBI refinement of bonded interactions, the distributions of CG beads corresponding to the bonded interactions (i.e., the distribution of bond lengths, angles, and dihedrals) were in excellent agreement with equivalent distributions obtained by CG-mapping the reference all-atom simulations. Next, nonbonded interaction potentials were refined through the IBI procedure applied to the 1−3 excluded pair distribution functions of the P and B beads; the bonded potentials were kept fixed. The IBI refinement of the nonbonded interactions yielded a CG model that produced pair distribution functions of the beads that were in excellent agreement with equivalent distributions obtained by CG-mapping the reference all-atom simulations; the agreement between bonded distributions was maintained. All CG simulations were performed using a custom version of the

MD software NAMD.[43] Details of the IBI refinement, final potentials, and distributions (along with the target distributions extracted from all-atom simulations) are provided in the Supporting Information.

Having completed the "bottom-up" stage of parametrization, the radius of gyration—a representation of the size of a molecule—was determined for a dT_{60} molecule using the 100 and 1000 mM parametrizations of the CG model. The radius of gyration was found to be 89% and 75% of the experimentally measured values (44.6 and 38.2 Å).[44] This disagreement likely originates from the imperfections of the all-atom model but may also be caused by the finite size of the all-atom reference system. Thus, we further refined the non-bonded potentials of our CG model until agreement with experimentally measured radii of gyrations was reached. For this "top-down" refinement, the nonbonded potential describing the interaction of the P beads was systematically altered by adding or subtracting a Yukawa potential of the appropriate Debye-length value, see Supporting Information for details. Upon completion of this procedure, the radius of gyration obtained in CG simulations agreed well with that measured in experiments across a broad range of polymer lengths and at both ion concentrations, see Figure 2.

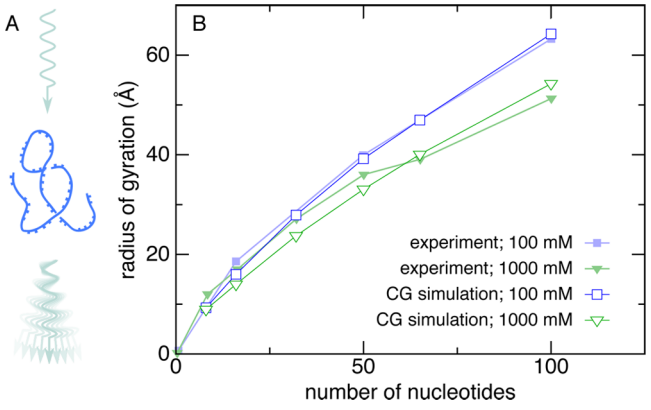

Figure 2. Radius of gyration, R_g, of a thymine homopolymer versus the homopolymer length. (A) Illustration of the experimental method, small-angle X-ray scattering, used to measure R_g. (B) Radius of gyration as a function of the polymer length. Good agreement was obtained between experimental measurements (filled symbols) and coarse-grained simulation (open symbols) under NaCl concentrations of 100−125 mM (blue squares) and 1000−1025 mM (green triangles). Experimental data were extracted from Sim et al.[44]

Without any further refinement of the model, the simulated force−extension dependence of a dT_{200} molecule was in excellent agreement with the experimentally measured dependence of one strand of λ-phage DNA (48 500 nts) under high applied force and similar ionic conditions,[45] see Figure 3. Similar simulations were performed using two"top-down" CG models 3SPN.2[27] and oxDNA,[31] see Supporting Information for details of these simulations. Our model, which was optimized specifically for ssDNA, performs extremely well for dT_{200} if compared to the 3SPN.2 model. Comparison with the oxDNA model is not entirely possible because that model was parametrized for 500 mM monovalent electrolyte. In the high force regime (above 20 pN), where electrolyte conditions are not expected to influence the extension of ssDNA,[46] the oxDNA model fits the experimental data well.

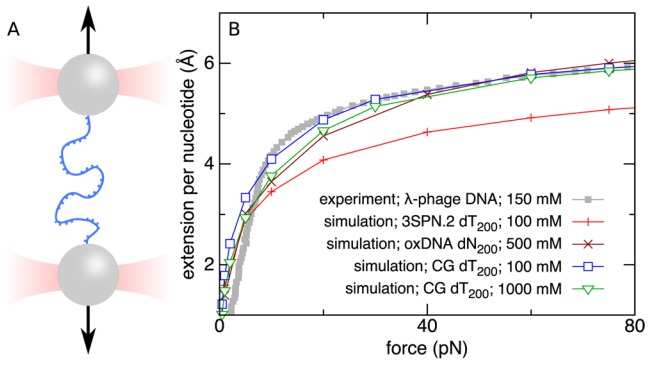

Figure 3. Simulated and measured force−extension dependence of ssDNA. (A) Illustration of the experimental method used to apply the force and measure the extension. Double-stranded λ-phage DNA (48.5 kbp) was caught between two beads in a dual optical trap. Melting and washing off the complementary DNA strand allowed the force−extension curve of the remaining strand to be determined. (B) Force−extension curve of ssDNA obtained through CG simulations and experiment. Data obtained using our CG model (open symbols) are in good agreement with experimental results[45] (filled symbols) at high force and both NaCl concentrations. Quantitative comparison at low force is not possible because of the secondary structure of λ-phage DNA that shortens DNA extension in the experiment. For comparison, we present force−extension dependence of dT_{200} in 100 mM electrolyte obtained using the 3SPN.2 model[27] and of 200 base-average nucleotides in 500 mM electrolyte obtained using the oxDNA model.[31]

At forces below ∼10 pN, secondary structures form in λ-phage DNA, reducing its extension if compared to poly(dT). In one experimental study, glyoxal was used to chemically denature λ-phage DNA, allowing the authors of that study to probe the low-force extension of ssDNA in the absence of secondary structure formation.[46] Unfortunately, the denaturation process may have introduced chemical cross-links so that the absolute length of the ssDNA molecule was unknown, precluding comparison of absolute extension per nucleotide. Nevertheless, after dividing the extension values by the extension at 20 pN for each measurement, the simulated extension of dT_{200} was in good agreement with the experimentally measured extension across 2 orders of magnitude of the applied force, see Figure 4. The 3SPN.2 and oxDNA models also agree well with the rescaled force−extension curves.

The use of long, mixed-sequence DNA molecules in previous experimental studies of ssDNA elasticity[45,46] complicates direct comparison with the simulation data. To validate our CG model for very short, chemically unmodified DNA fragments we turned to advanced single molecule techniques. Specifically, we used fluorescence resonance energy transfer (FRET) detection to measure the extension of a dT_{14} molecule under tension applied by an optical trap,[47] see Figure 5A. In this assay, the DNA construct was immobilized on a poly(ethylene glycol) coated glass slide at one end using the biotin−neutravidin interaction. The other end of the construct was connected to a micrometer polysterene bead via a λ-phage DNA linker. The preparation of the DNA construct is described in detail in the Supporting Information. The bead was optically trapped, putting the DNA construct under tension. A pair of dyes (Cy3 and Cy5) was attached at the two ends of the dT_{14} fragment to provide a FRET signal that effectively allowed the

dx.doi.org/10.1021/ct500193u | J. Chem. Theory Comput. 2014, 10, 2891−2896

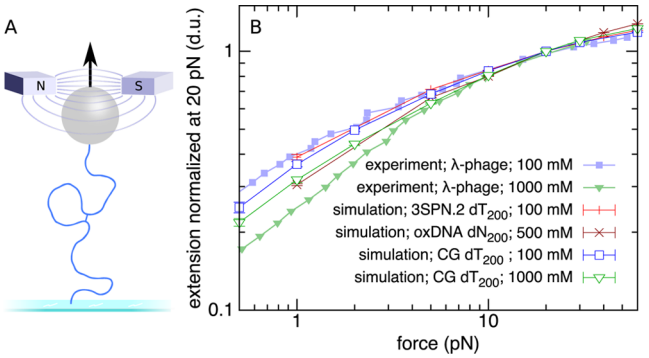

Figure 4. Simulated and measured force–extension dependence of ssDNA. (A) Illustration of the experimental method used to apply the force and measure the extension. Chemically denatured λ-phage DNA was stretched between a glass slide and a magnetic bead. The denaturant, which prevents formation of secondary structure, also introduced cross-links between parts of the DNA, which made determination of the absolute extension not possible. (B) Force–extension curve of ssDNA obtained through CG simulations and experiment. Good agreement was observed between experimental measurements[46] (filled symbols) and coarse-grained simulations performed using our model (open symbols), the 3SPN.2 model[27] in 100 mM electrolyte and the oxDNA model[31] in 500 mM electrolyte.

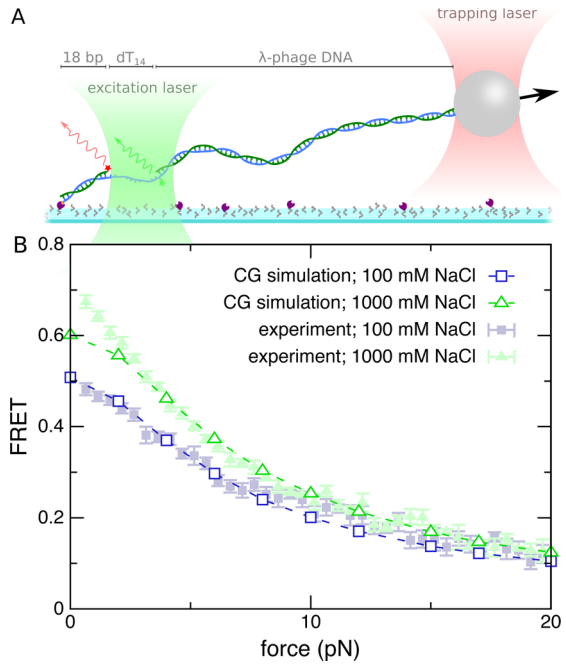

Figure 5. Force–extension dependence of dT_{14}. (A) Illustration of the experimental method used to simultaneously stretch DNA and measure the FRET signal. A green laser excites the Cy3 donor dye; some energy is nonradiatively transferred to the Cy5 acceptor dye. The amount of energy transferred, the FRET efficiency, is related to the distance between the dyes. An optical trap applies tension. (B) FRET efficiency vs force observed in the experiment (filled symbols) and calculated from the CG simulations of dT_{14} under tension (open symbols). The following expression was used to compute FRET based on the distance r between the terminal P beads: $\langle 1/(1 + ((r + \delta)/R_0)^6)\rangle$, where R_0 = 60 Å is the Förster distance and δ = 22 Å is a constant factor associated with the physical dimensions and placement of the dyes. The angle brackets represent an average over the simulation trajectory. The agreement between simulation and experiment was good at 100 (blue squares) and 1000 mM (green triangles).

end-to-end distance to be monitored as a function of the applied force.

Figure 5B shows the FRET vs force curves obtained at two different salt conditions as described in the Supporting Information. As the tension increases, the FRET signal decreases, indicating extension of the dT_{14} fragment of the construct. In the low-force regime, the FRET values depend on the ionic conditions but converge in the high-force regime (>10 pN). The low-force FRET is larger under high NaCl concentration, implying greater compaction of ssDNA caused by stronger electrostatic screening. This observation is consistent with our earlier work[48] and with the observed shrinking of ssDNA under high salt conditions.[44] At high force, the FRET curves converge as the extension of the polymer approaches its contour length. The FRET efficiency computed from our CG simulations of dT_{14} under tension is in good agreement with the experimental FRET traces at 100 and 1000 mM NaCl, see Figure 5B.

From a practical perspective, our CG model permits microsecond-per-day simulations of hundreds of nucleotides on a single processor core. One should note that dynamics are usually enhanced in coarse-grained simulations compared to all-atom, for example, due to smoothing of the free energy landscape.[49] For dT_{60} using our model, each CG nanosecond corresponds to ∼80 real-world nanoseconds. However, we found that the enhancement for a DNA molecule depends on its length, see the Supporting Information for details. The only nonstandard features of an MD code required to perform CG simulations using our model are tabulated bonded and nonbonded potentials. It must also be possible to apply bonds by bead index rather than bead type as the P_n–B_n and B_n–P_{n+1} potentials differ.

The most significant limitations of our model are 3-fold. First, the model is currently limited to simulations of unstructured ssDNA, such as poly(dT). Second, the base beads are spheres that lack orientation that may be important for accurate modeling of base-pairing and base-stacking in duplex DNA. However, anisotropic base–base interactions require additional computation and reduce portability of the model. Finally, our model lacks a description of hydrodynamic interactions, which makes interpretation of kinetic information difficult, see the Supporting Information for details.

Despite its simplicity, our CG model provides a structurally accurate portrayal of a poly(dT) molecule across a wide range of polymer lengths, applied tensions and ion concentrations. This makes our model immediately suitable for CG studies of ssDNA systems where sequence-specific effects, including base-pairing and strong adenosine stacking,[50] can be neglected. Thus, our model should be best suited to the simulation of ssDNA comprising thymine and cytosine nucleotides. We have already used a preliminary version of our model to study the effect of local heating on the process of ssDNA transport through a solid-state nanopore.[51]

With only two sites per nucleotide, extensions to the model can be easily made. For example, it was trivial to create a toy model of double-stranded DNA by adding a set of harmonic potentials to describe base-paring of two CG DNA strands, Figure 6. The physical properties of the resulting dsDNA model could be easily adjusted by changing the strength of the interstrand harmonic potentials. Other extensions are also possible. For example, by representing proteins using a grid-based potential, one may study the interaction between a CG DNA molecule and a DNA-binding protein. Our simple,

dx.doi.org/10.1021/ct500193u | J. Chem. Theory Comput. 2014, 10, 2891–2896

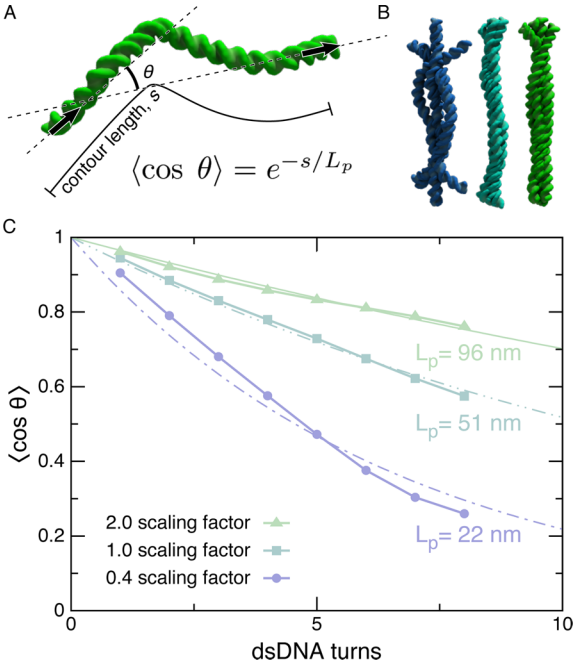

Figure 6. Custom flexibility CG model of dsDNA. (A) Definition of the persistence length L_p. The persistence length is a measure of a polymer's flexibility that can be directly derived from a simulation trajectory. (B) Representative conformations of a 100-bp dsDNA fragment having different parametrization of interstrand interactions (a = 0.4, blue; 1.0, teal; and 2.0, green). In our dsDNA model, parameter a defines the strength of interstrand interactions. Individual DNA strands are described using our CG model of ssDNA. (C) Angular correlation of two DNA fragments versus distance between the fragments. An exponential fit reveals the persistence length. Colors are as in B. The flexibility of dsDNA can be controlled by changing the scaling factor a. The harmonic restraints used to enforce base-pairing preclude the possibility of melting. Additional details are provided in the Supporting Information.

computationally efficient, yet accurate model of ssDNA is a step toward a complete physical model of the DNA processing machinery of a living cell.

■ ASSOCIATED CONTENT

Ⓢ Supporting Information

Detailed descriptions of the all-atom and CG simulations, refinement of the CG potential, and single-molecule experiments; discussion of the time scale of CG simulations; and plots of all CG potentials and associated distributions from CG and all-atom simulations. This material is available free of charge via the Internet at http://pubs.acs.org/.

■ AUTHOR INFORMATION

Corresponding Author

*E-mail: aksiment@illinois.edu.

Notes

The authors declare no competing financial interest.

■ ACKNOWLEDGMENTS

This work was supported by the grants from the National Science Foundation (PHY-0822613 and DMR-0955959) and the National Institutes of Health (R01-HG007406, R01-GM065367, and P41-GM104601). The authors gladly acknowledge supercomputer time provided through XSEDE Allocation Grant MCA05S028 and the Taub Cluster (UIUC).

■ REFERENCES

(1) De Santis, P.; Scipioni, A. *Phys. Life Rev.* **2013**, *10*, 41−67.
(2) Ghirlando, R.; Felsenfeld, G. *Biopolymers* **2013**, *99*, 910−915.
(3) Zhang, D. Y.; Seelig, G. *Nat. Chem.* **2011**, *3*, 103−113.
(4) Pestryakov, P. E.; Lavrik, O. I. *Biochemistry (Moscow)* **2008**, *73*, 1388−1404.
(5) Waga, S.; Stillman, B. *Annu. Rev. Biochem.* **1998**, *67*, 721−751.
(6) Zou, L.; Elledge, S. J. *Science* **2003**, *300*, 1542−1548.
(7) Chase, J. W.; Williams, K. R. *Annu. Rev. Biochem.* **1986**, *55*, 103−136.
(8) Seeman, N. C. *Annu. Rev. Biochem.* **2010**, *79*, 65−87.
(9) Rothemund, P. *Nature* **2006**, *440*, 297−302.
(10) Dietz, H.; Douglas, S. M.; Shih, W. M. *Science* **2009**, *325*, 725−30.
(11) Nykypanchuk, D.; Maye, M. M.; van der Lelie, D.; Gang, O. *Nature* **2008**, *451*, 549−552.
(12) Maune, H. T.; Han, S.-P.; Barish, R. D.; Bockrath, M.; Iii, W. A. G.; Rothemund, P. W. K.; Winfree, E. *Nat. Nanotechnol.* **2010**, *5*, 61−66.
(13) Gu, H.; Chao, J.; Xiao, S.-J. J.; Seeman, N. C. *Nature* **2010**, *465*, 202−5.
(14) Pérez, A.; Luque, F. J.; Orozco, M. *Acc. Chem. Res.* **2012**, *45*, 196−205.
(15) Dror, R. O.; Dirks, R. M.; Grossman, J. P.; Xu, H.; Shaw, D. E. *Annu. Rev. Biophys.* **2012**, *41*, 429−452.
(16) Yoo, J.; Aksimentiev, A. *Proc. Natl. Acad. Sci. U. S. A.* **2013**, *110*, 20099−20104.
(17) Laughton, C. A.; Harris, S. A. *Wiley Interdiscip. Rev.: Comput. Mol. Sci.* **2011**, *1*, 590−600.
(18) Guy, A. T.; Piggot, T. J.; Khalid, S. *Biophys. J.* **2012**, *103*, 1028−1036.
(19) Uzawa, T.; Isoshima, T.; Ito, Y.; Ishimori, K.; Makarov, D. E.; Plaxco, K. W. *Biophys. J.* **2013**, *104*, 2485−2492.
(20) Saunders, M. G.; Voth, G. A. *Annu. Rev. Biophys.* **2013**, *42*, 73−93.
(21) Potoyan, D. A.; Savelyev, A.; Papoian, G. A. *WIREs Comput. Mol. Sci.* **2013**, *3*, 69−83.
(22) Doye, J. P. K.; Ouldridge, T. E.; Louis, A. A.; Romano, F.; Sulc, P.; Matek, C.; Snodin, B. E. K.; Rovigatti, L.; Schreck, J. S.; Harrison, R. M.; Smith, W. P. J. *Phys. Chem. Chem. Phys.* **2013**, *15*, 20395−20414.
(23) Maciejczyk, M.; Spasic, A.; Liwo, A.; Scheraga, H. A. *J. Comput. Chem.* **2010**, *31*, 1644−1655.
(24) Gopal, S. M.; Mukherjee, S.; Cheng, Y.-M.; Feig, M. *Proteins: Struct., Funct., Bioinf.* **2010**, *78*, 1266−1281.
(25) Cragnolini, T.; Derreumaux, P.; Pasquali, S. *J. Phys. Chem. B* **2013**, *117*, 8047−8060.
(26) Dans, P. D.; Zeida, A.; Machado, M. R.; Pantano, S. *J. Chem. Theory Comput.* **2010**, *6*, 1711−1725.
(27) Hinckley, D. M.; Freeman, G. S.; Whitmer, J. K.; de Pablo, J. J. *J. Chem. Phys.* **2013**, *139*, 144903.
(28) Šulc, P.; Romano, F.; Ouldridge, T. E.; Rovigatti, L.; Doye, J. P. K.; Louis, A. A. *J. Chem. Phys.* **2012**, *137*, 135101.
(29) Knotts, T. A.; Rathore, N.; Schwartz, D. C.; de Pablo, J. J. *J. Chem. Phys.* **2007**, *126*, 084901.
(30) Sambriski, E. J.; Schwartz, D. C.; de Pablo, J. J. *Biophys. J.* **2009**, *96*, 1675−1690.
(31) Ouldridge, T. E.; Louis, A. A.; Doye, J. P. K. *J. Chem. Phys.* **2011**, *134*, 085101.
(32) De Biase, P. M.; Solano, C. J. F.; Markosyan, S.; Czapla, L.; Noskov, S. Y. *J. Chem. Theory Comput.* **2012**, *8*, 2540−2551.
(33) Morriss-Andrews, A.; Rottler, J.; Plotkin, S. S. *J. Chem. Phys.* **2010**, *132*, 035105.
(34) He, Y.; Maciejczyk, M.; Ołdziej, S.; Scheraga, H. A.; Liwo, A. *Phys. Rev. Lett.* **2013**, *110*, 098101.

(35) Savelyev, A.; Papoian, G. A. *Proc. Natl. Acad. Sci. U. S. A.* **2010**, *107*, 20340−20345.
(36) Hsu, C. W.; Fyta, M.; Lakatos, G.; Melchionna, S.; Kaxiras, E. *J. Chem. Phys.* **2012**, *137*, 105102.
(37) Xia, Z.; Gardner, D. P.; Gutell, R. R.; Ren, P. *J. Phys. Chem. B* **2010**, *114*, 13497−13506.
(38) DeMille, R. C.; Cheatham, T. E.; Molinero, V. *J. Phys. Chem. B* **2011**, *115*, 132−142.
(39) Chen, H.; Meisburger, S. P.; Pabit, S. A.; Sutton, J. L.; Webb, W. W.; Pollack, L. *Proc. Natl. Acad. Sci. U. S. A.* **2012**, *109*, 799−804.
(40) Hart, K.; Foloppe, N.; Baker, C. M.; Denning, E. J.; Nilsson, L.; MacKerell, A. D. *J. Chem. Theory Comput.* **2012**, *8*, 348−362.
(41) Yoo, J.; Aksimentiev, A. *J. Phys. Chem. Lett.* **2012**, *3*, 45−50.
(42) Yoo, J.; Aksimentiev, A. *J. Phys. Chem. B* **2012**, *116*, 12946−12954.
(43) Phillips, J. C.; Braun, R.; Wang, W.; Gumbart, J.; Tajkhorshid, E.; Villa, E.; Chipot, C.; Skeel, R. D.; Kale, L.; Schulten, K. *J. Comput. Chem.* **2005**, *26*, 1781−1802.
(44) Sim, A.; Lipfert, J.; Herschlag, D.; Doniach, S. *Phys. Rev. E* **2012**, *86*, 1−5.
(45) Smith, S. B.; Cui, Y.; Bustamante, C. *Science* **1996**, *271*, 795−799.
(46) Saleh, O.; McIntosh, D.; Pincus, P.; Ribeck, N. *Phys. Rev. Lett.* **2009**, *102*, 068301.
(47) Hohng, S.; Zhou, R.; Nahas, M. K.; Yu, J.; Schulten, K.; Lilley, D. M. J.; Ha, T. *Science* **2007**, *318*, 279−83.
(48) Murphy, M. C.; Rasnik, I.; Cheng, W.; Lohman, T. M.; Ha, T. *Biophys. J.* **2004**, *86*, 2530−2537.
(49) Zwanzig, R. *Proc. Natl. Acad. Sci. U. S. A.* **1988**, *85*, 2029−2030.
(50) McIntosh, D. B.; Duggan, G.; Gouil, Q.; Saleh, O. A. *Biophys. J.* **2014**, *106*, 659−666.
(51) Belkin, M.; Maffeo, C.; Wells, D. B.; Aksimentiev, A. *ACS Nano* **2013**, *7*, 6816−6824.